Transport in Porous Media (2019) 129:431–448
https://doi.org/10.1007/s11242-019-01297-9

Establishing Framework for 3D Printing Porous Rock Models in Curable Resins

Sergey Ishutov[1]

Received: 27 February 2019 / Accepted: 22 May 2019 / Published online: 27 May 2019

Abstract
Stereolithographic 3D printing is of paramount interest for researchers studying porous media because it is possible to use resins with a wide range of physical and chemical properties. Currently, these properties can be designed and adjusted to model the interaction of solids with fluids occupying the pore space, which is not feasible with natural materials. This ability enables replicating the pore network geometry of natural rocks as well as tuning the wettability of pore network surfaces. This study presents analysis of uncured liquid resins and porous rock models 3D-printed in those resins to establish the accuracy of the stereolithographic 3D printer in repeatedly printing the same pore network, as well as the fidelity of transport properties (e.g., porosity, pore sizes, wettability) to the model design. Viscosity of uncured resins was measured to predict the physical properties of the resulting cured models. A digital model of Fontainebleau sandstone was 3D-printed at three magnifications (15-, 23-, and 30-fold) from the original tomographic volume of 1 mm^3 and in six resins (black, gray, clear, white, green, and yellow). The models were validated using the following techniques: helium pycnometry (for porosity); mercury porosimetry (for pore-throat size); and drop shape analyzer (for contact angles). Validation tests showed that green resin had the highest accuracy in replicating the rock's pore network. White, yellow, and gray resins produced models with moderate accuracy with respect to their transport properties. Black and clear resins had the lowest accuracy and would need further analysis of their physical and chemical properties to be useful in reservoir rock replication.

Keywords 3D printing · Resin · Flow · Wettability · Geomechanics

1 Introduction

Investigation of transport and geomechanical processes that occur at pore scale is important to understanding of many natural phenomena of fluid-bearing porous media (e.g., hydrocarbon reservoirs and groundwater aquifers). Sustainable recovery of hydrocarbons and groundwater

✉ Sergey Ishutov
ishutov@ualberta.ca

[1] Department of Civil and Environmental Engineering, Donadeo Innovation Centre for Engineering, University of Alberta, 9211-116 Street NW, Edmonton, AB T6G 1H9, Canada

from reservoir formations as well as CO_2 sequestration in the subsurface requires prediction of the multiphase flow in complex pore networks at high temperatures and pressures. Imaging and nondestructive analysis of porous media have become available through the field of "digital rock physics," where rock properties are simulated numerically (e.g., Dvorkin et al. 2008; Andrä et al. 2013; Blunt et al. 2013). Three-dimensional (3D) printing is an emerging technology for characterization of porous media that enables the manufacture of physical proxies of pore networks from digital models (Ishutov et al. 2018a, b; Ishutov and Hasiuk 2018). Proxies allow us to experimentally test petrophysical properties (e.g., porosity and permeability) that can complement digital rock analysis. This advantage arises from the ability to design material properties of proxies (e.g., chemical, optical, mechanical, thermal, or electrical) to model the behavior of natural materials under more controlled experimental conditions.

Stereolithographic (SLA) 3D printing has been used in the characterization of two model types: (1) microfluidic devices and micromodels ("2.5D models") and (2) full volumetric models (e.g., solid or porous proxies; "3D model"). SLA uses curable resins that are solidified (or cured) with laser light, layer by layer (Ishutov et al. 2018b). Micromodels provide one way to visualize pore-scale flow as well as reactive and non-reactive transport processes, despite limitations in channel size stemming from the 3D printer's resolution (Gunda et al. 2011; Xu et al. 2014). These miniaturized, artificial porous media (often called "reservoir on a chip") are useful tools for studies of rock and fluid properties at pore scale, because the pore structure can be controlled, and flow processes can be directly visualized (Song et al. 2014; Zarikos et al. 2018).

Micromodels are simple renderings of a rock's pore network, but it is necessary to perform flooding experiments, similar to those in reservoir engineering, to interpret wettability and permeability of rock formations. Current advances in reservoir-on-a-chip devices include chemical coating of surfaces to mimic the wettability of natural rocks and embedding sensors to track pressure inside microchannels. Gerami et al. (2016) showed application of polydimethylsiloxane (PDMS) microfluidic devices 3D-printed from tomographic data in understanding the relationship between coal cleat structure and relative permeability of methane gas. Manzano et al. (2017) developed a specific resin that could produce surfaces with active polymer sites and controlled wettability. Alzahid et al. (2018) developed a novel technique that attached rock minerals to PDMS creating microfluidic devices with surfaces that mimicked closely natural geological materials. Zarikos et al. (2018) reported a micromodel with integrated fiber optic sensors to enable the measurement of fluid pressure at pore scale.

Recent studies on deformation of micromodels and 3D-printed volumes showed visualization and experimentation with single and multiphase flow. Munro et al. (2015) demonstrated a method of 3D printing with an infused PDMS elastomer to measure mechanical deformations with controlled pore architecture. Zhou and Zhu (2017) used a curable resin to simulate geomechanical behavior of rocks, which was the most suitable 3D printing material for mimicking brittle and hard rocks. Ju et al. (2017) presented a method of experimentally visualizing frozen-stress fields in the 3D structures of porous solids using a photoelastic resin. Zhou et al. (2019) used SLA to 3D-print resin-based artificial rocks containing penny-shaped 3D internal fractures to investigate the influence of fracture number and angle on the volumetric fracturing behavior.

Integration of numerical simulations and resin-based models with intrinsic rock geometric features is a way to design the transport and mechanical properties of rocks. Bacher et al. (2014) and Matsumura et al. (2017) described the use of X-ray tomography imaging of natural gravel specimens to create repeatable gravel size resin models. The resulting models

had particle geometry and interparticle bonds that were a function of the resolution of both the tomographic scanner and the 3D printer expanding the capabilities for numerical calculation of porosity and permeability and hence flow simulation. Zhu et al. (2018) combined SLA with the X-ray tomography to replicate natural volcanic rocks using a transparent resin. This study showed the feasibility for both 3D printing and 3D numerical modeling to successfully replicate the internal fractures and microstructures identical to those of the natural volcanic rock. While models 3D-printed in curable resins provide a promising means to replicate and visualize the geometry of porous media and to understand the influence of pore network geometry and surface physics on transport and mechanical behavior of rocks under different experimental conditions, each resin requires characterization of its physical and chemical properties prior to manufacturing rock proxies.

The chemical composition of a curable resin defines the mechanical behavior of the resulting cured model 3D-printed via SLA. A typical SLA resin includes oligomers, monomers, and photoinitiators (Ogawa and Hasegawa 2005). Resin polymerization (solidification) occurs when a laser beam passes through a layer of the liquid resin. Key parameters for prediction of mechanical properties and accuracy of 3D-printed models in the resin are temperature, humidity, and pressure during polymerization because they affect resin viscosity. Viscosity is the property that determines the mobility of molecules within a resin. During polymerization, if viscosity increases through the formation and growth of monomer and oligomer chains, it can result in decreased molecular movement. This limited molecular movement leads to completion of polymerization. Preheating the resin prior to 3D printing allows the polymers to become thermally agitated and increase molecular motion, reducing viscosity. While an increase in temperature and pressure increases strength and stiffness of the resin, increase in humidity reduces surface hardness of the resin (Ayub et al. 2014).

This study characterizes the petrophysical properties of six curable resins prior to and after SLA printing. This characterization is novel to routine procedures of porous rock analysis because it is aimed at establishing factors that affect the accuracy of rock proxies in relation to transport and geomechanical properties. The first part of this study involves analysis of physical properties of liquid resins from vendor's material data sheets and validation tests. Due to proprietary composition of these resins from a vendor, the only parameter that can be determined experimentally without changing their initial state is viscosity. Viscosity was measured at 25 °C (normal conditions) and at 35 °C (preheating before 3D printing). Interaction of water with 3D-printed surfaces of resin-based models was characterized using the sessile drop method. The second part involved 3D printing proxies of Fontainebleau sandstone from a 1 mm^3 digital tomographic volume (Lindquist et al. 2000) at three magnifications (15-, 23-, and 30-fold). Fidelity of rock proxies was tested by helium pycnometry and mercury porosimetry (that was never performed on any rock proxy 3D-printed in curable resins). The objectives of this study were: (1) to investigate whether physical properties of uncured resins can be used to predict accuracy of the resulting 3D-printed models; (2) to identify the resin that has the highest accuracy for manufacture of porous rock models with known porosity and pore-throat size distribution; and (3) to determine the parameters of cured and uncured resins that affect transport and geomechanical properties of rock proxies.

2 Materials and Methods

Methods for determination of resin properties involved analysis of vendor's material data sheets and experimental tests to validate these properties. For uncured resins, the properties

tested included viscosity and density. For cured (3D-printed) resins, density, porosity, pore-throat size distribution, and contact angles with water were investigated. In total, six resins (black, gray, clear, white, green, and yellow) were used to produce proxies on a FormLabs Form2 SLA printer (Sommerville, Massachusetts, USA) (Table 1).

2.1 Resin Types

Black, gray, clear, and white resins are called "standard resins" in the vendor's material data sheets and have the same density (1.09–1.12 g/cm^3) and viscosity (850–900 cps measured at 25 °C). The exact composition of resins is proprietary to the vendor, but material data sheets list their components as methacrylated monomers and oligomers, acrylated monomers, color pigments, and photoinitiators (Table 1). While pigments determine the color of each resin, properties of cured resins are independent of this color. 3D printing with these resins starts when the temperature of the liquid resin in the tank reaches 25 °C. A green resin has the same composition and density as the standard resins, but its viscosity is 970 cps (measured at 35 °C). 3D printing for the green resin starts when its tank temperature reaches 35 °C. The tough resin is designed to simulate mechanical properties of acrylonitrile butadiene styrene plastic (e.g., tensile strength and modulus; FormLabs). A yellow (high-temperature) resin has the same density as the other five resins, but it is slightly different in composition, lacking methacrylated monomers. The viscosity of the yellow resin is 600 cps (measured at 25 °C). The printing for this resin starts when its tank temperature is 25 °C. A high-temperature resin has the highest heat deflection temperature among other resins (289 °C at 0.45 MP), which makes it the stiffest resin tested in this study (FormLabs).

2.2 Viscosity Tests

A Rheosys Merlin II rheometer (Structure Lab, Iowa State University, Ames, USA; Fig. 1a) was used to quantify the viscosity of six resins at two temperatures: 25 °C and 35 °C. Testing at these temperatures was required to verify if resins stored and printed at these temperatures could conform to viscosity specified in material data sheets and to investigate whether environmental conditions of the printing process (pressure and humidity) could affect the resulting accuracy of proxies. 50 ml of a liquid resin was loaded into the chamber where it was preheated to the specified temperature (Fig. 1b). A spindle with a metal cone rotated at the speed range of 0.2–100 rotations per minute (rpm), with 1-rpm increments. Viscosity for each resin in this study was reported as the average of these rotations after the speed reached a constant resin drag. The viscous drag of the resin (shear stress) against the rotating spindle was measured by the resin current (sensed by transducer) required to maintain the incremental speed. Tests were performed under the ambient temperature of 23 °C, humidity of 60%, and atmospheric pressure of 103,013.9 Pa, and viscosity accuracy was 1%.

2.3 3D Printing

A stereolithographic 3D printer (FormLabs Form2, GeoFabLab, Iowa State University, Ames, USA) was used in his study to manufacture proxies of Fontainebleau sandstone. A liquid resin loaded in the tank was cured by ultraviolet laser that passed through the bottom of the tank. Once the layer was solidified on the build platform, the build platform raised by the layer height (50 μm) and the next layer was built in the same manner until all layers were

Table 1 Chemical and physical properties of liquid (uncured) resins provided by the vendor (Formlabs)

Resin	Trade name	Components	Viscosity (cps)	Heat deflection temperature at 0.45 MPa (°C)	Tensile strength (MPa)	Flexural modulus (GPa)
Black Gray White	Standard	Methacrylated oligomers, Methacrylated monomer, Photoinitiator, Pigments, Specialty additives	850–900 (at 25 °C)	49.7	38	1.25
Clear		Same as above three resins, with no specialty additives				
Green	Tough	Same as above four resins, with no pigments or specialty additives and including acrylated monomers,	970 (at 35 °C)	40.4	34.7	0.6
Yellow	High temperature	Methacrylated oligomers, Acrylated monomers, Photoinitiator	600 (at 25 °C)	43.6	20.9	2.62

The percentage content of each component in resins is proprietary to the vendor. The following properties are the same for all resins: density range—1.09–1.12 g/cm^3; soluble in organic solvents and very slightly soluble in water; flash point > 93 °C

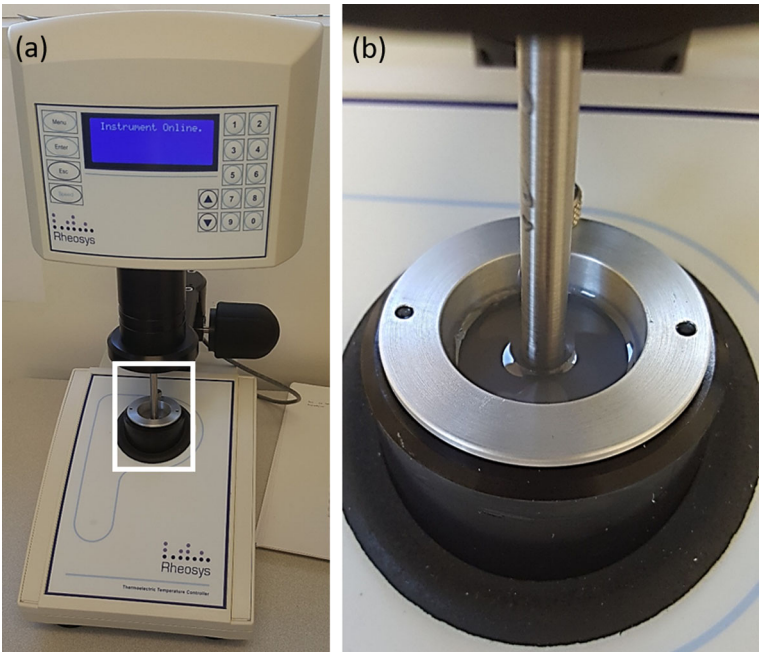

Fig. 1 Photographs of Rheosys Merlin II rheometer. **a** Front view of the rheometer. **b** Chamber with liquid resin and agitating cone. Liquid resin is loaded into the chamber and heated up to 25 °C and 35 °C before the cone is rotating at the specified speed. The viscous drag of the resin against the rotating cone is measured by the current required to maintain the speed

printed. More details on printing and post-processing procedures can be found in Ishutov et al. (2018b).

For porous proxies, the layer thickness determines the minimum size of a solid feature and pore that can be 3D-printed and is linked to the laser spot size of the SLA 3D printer (Ishutov et al. 2018b). According to vendor's specifications, not all resins in this study could match the smallest layer thickness of the printer (25 μm); hence, proxies were printed with 50-μm layers (the layer thickness supported for all resins) to maintain consistency among all models. Fontainebleau sandstone proxies were printed from 1 mm^3 tomographic volume (Fig. 2a; Lindquist et al. 2000) at three magnifications: 15-, 23-, and 30-fold to match the minimum resolution of the printer and resin specifications (Fig. 2b–g; Ishutov et al. 2018b). Porosity measured from the original tomographic volume was 12.7%, and mean pore-throat diameter was 30.4 μm (Ishutov et al. 2018b). Bulk volume and porosity were calculated from tomographic volume; resin density was provided by material data sheets; and mass was calculated from tomographic volume and material density (Table 1). All proxies were 3D-printed under the ambient temperature of 23 °C, humidity of 60%, and atmospheric pressure of 103,012.6 Pa.

2.4 Sessile Drop Method

A video-based drop shape analyzer (OCA 25, Data Physics, Germany) with built-in SCA 20 software (V.4.5.20) was used for the contact angle measurement of printed proxy surfaces

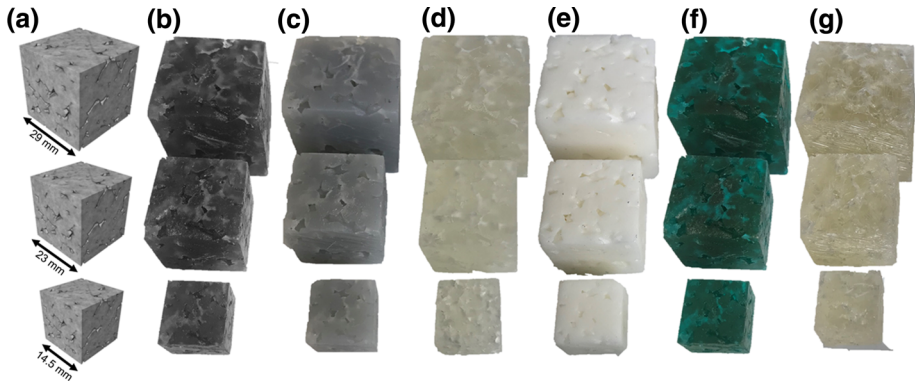

Fig. 2 Proxies of Fontainebleau sandstone 3D-printed in six resins. From left to right: **a** Original tomographic volume of Fontainebleau sandstone, porosity is 12.7%; proxies 3D-printed in the following resins: **b** black; **c** gray; **d** clear; **e** white; **f** green; **g** yellow. For each resin and tomographic models, from bottom to top, the magnifications are 15-, 23-, and 30-fold

with water (AMD Lab, Iowa State University, Ames, USA). The sessile drop method provided measurements under the ambient temperature of 25 °C, humidity of 65%, and atmospheric pressure of 103,013.2 Pa, following the guidelines of ASTM-D7334-08 (2013). Samples for this test were disks (20 mm in diameter and 10 mm in height) 3D-printed in each resin (Fig. 3a). A droplet of 2 μL of deionized water was extruded from a micro-syringe (Fig. 3b) onto the proxy surface. The high-resolution camera (Fig. 3c) captured 1000 frames of the proxy surface with water. The contact angles were measured as a mean value for all frames by the built-in software of the drop shape analyzer.

2.5 Helium Pycnometry

Helium pycnometry was used to measure porosity and density of Fontainebleau sandstone proxies. Micromeritics Accupyc II 1340 helium pycnometer (GeoFabLab, Iowa State University, Ames, USA) was used to determine the volume of the solid phase in proxies (analogous to "grain" volume in natural rocks) that can be accessed by a helium molecule (diameter = 0.062 nm). Pore volume was calculated by subtracting the material volume from the bulk volume (as measured by calipers). Porosity was calculated as the ratio of pore volume to bulk proxy volume.

2.6 Mercury Porosimetry

Mercury intrusion porosimetry was performed only on 15-fold proxies due to size limitations of the sample cell (23-mm^3 cylinder) and pore-throat size range (5.6 nm to 500 μm) that could be measured. A Quantachrome Poremaster33 (GeoFabLab, Iowa State University, Ames, USA) was used for mercury porosimetry with pressures from 0 to 30 kpsi (~200 MPa), mercury contact angle of 140°, mercury temperature of 23 °C, interfacial tension of 480 dynes/cm^2, humidity of 55%, and atmospheric pressure of 103,012.4 Pa. A solid cube 3D-printed in the black resin with the same dimensions as the 15-fold magnification proxy (15 mm by 15 mm by 15 mm) was subjected to mercury intrusion porosimetry as a control sample to investigate intricate porosity between 3D-printed layers.

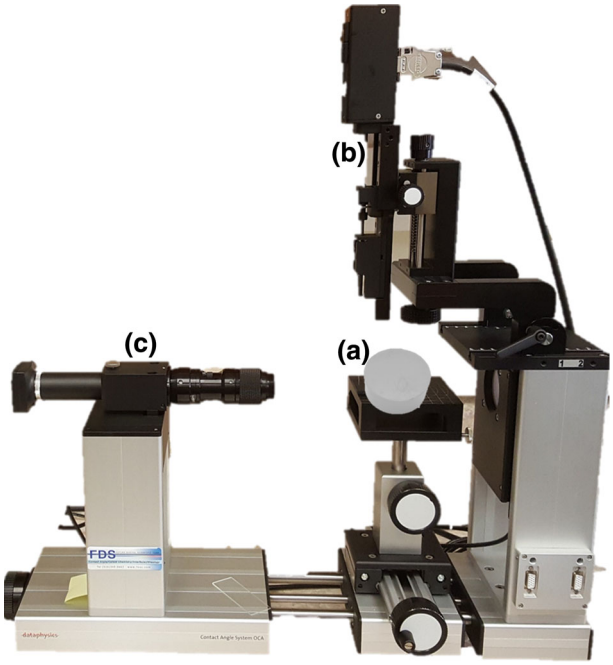

Fig. 3 Photograph of the drop shape analyzer (OCA 25, Data Physics, Germany). The sessile drop method is used to record the contact angle measurements at 25 °C (following the guidelines of ASTM-D7334-08). The 3D-printed sample (disk with 10 mm in height and 20 mm in diameter) is placed on the platform (**a**). A droplet of 2 μL of deionized water is dropped from a micro-syringe (**b**) to the sample surface. The high-resolution camera (**c**) captures 1000 frames of the sample surface, and the contact angles are measured by the built-in software

3 Results

The results contain an integrated analysis for resins in two states: (1) uncured liquid resins and (2) solid proxies 3D-printed from those resins. Despite composition, one of the major properties of liquid resins is viscosity, because it affects the physical properties of the resulting 3D-printed models. Physicochemical properties of resins, including density, wettability, and porosity, determine the resulting transport and geomechanical properties of the proxies. Ultimately, potential transport properties are evaluated through pore-throat size distribution that depends on the accuracy of the pore network geometry.

3.1 Viscosity of Uncured Resins

Viscosity measured on black, gray, clear, and white resins (836–898 cps) matched closely with the viscosity range (850–900 cps) provided by vendor's material data sheets for 25 °C (Fig. 4). The yellow (high-temperature) resin showed the highest deviation (~485 cps) from the vendor's material data sheets (~600 cps) among resins that were required to be printed at 25 °C. Viscosity of all resins, except for the green resin, decreased 2–3-fold at 35 °C (215–533 cps). The green (tough) resin was 3D-printed at 35 °C, and its viscosity (1033 cps)

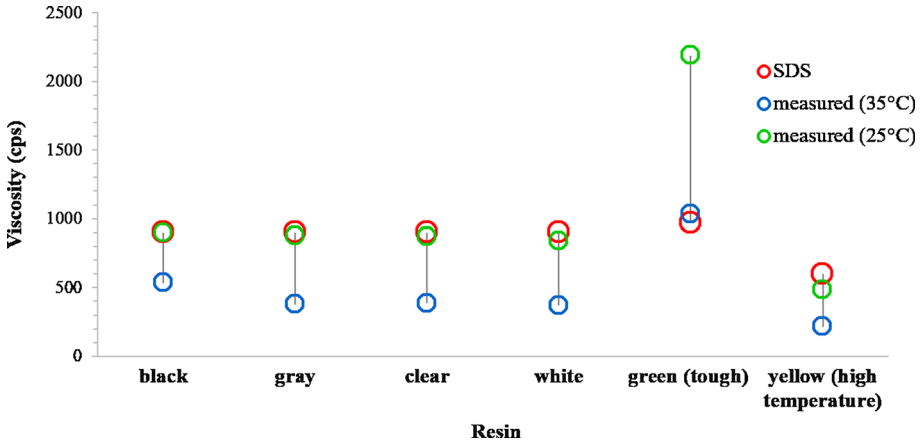

Fig. 4 Results of viscosity tests performed at Rheosys Merlin II rheometer. Viscosity was measured at 25 °C and 35 °C because resins are printed at these temperatures. SDS refers to vendor's material data sheets

conformed to vendor's data (970 cps). Similar to the other five resins, the viscosity of the green resin increased at 25 °C (~2187 cps).

3.2 Contact Angles of Proxy Surfaces with Water

Contact angle measurements showed two groups of proxies (Fig. 5): (1) proxies with contact angles close to 90° (black, gray, clear, and white resins) and (2) proxies with contact angles less than 50° (green and yellow resins). Deviation in contact angles and hence wettability of proxies printed in resins with similar density and viscosity indicated differences in their chemical composition. According to composition of resins provided by the vendor, green and yellow resins contained acrylated monomers that were absent in other four resins. Tough and high-temperature resins were more wetting to water and contained no air bubbles inside the water drop (Fig. 5e–f), unlike other resins (Fig. 5a–d). The surface of proxy 3D-printed in clear resin was not smooth as in other proxies (Fig. 5c) that could have affected the results of imaging and contact angle measurement.

3.3 Helium Porosity and Density

Results of helium pycnometry and caliper measurements of Fontainebleau sandstone proxies were analyzed in two manners: (1) comparison of bulk properties and porosity among each magnification in all resins and (2) comparison of repeatability of bulk properties and porosity of all magnifications in each resin. For 15-fold magnification, the helium porosity of the proxy 3D-printed in the green resin (10.05%) showed the closest match to the designed porosity (12.7%; Table 2). For 23-fold magnification, the white resin produced the proxy that most matched the designed tomographic porosity (10.54%). For 30-fold magnification, the gray resin was the closest to the tomographic porosity (12.43%). Deviation of helium porosity from designed porosity could have been affected by inaccuracy of bulk volumes 3D printed in each resin and insufficient resolution of the 3D printer to build all connected pores and pore throats. Because the printer's minimum resolution and post-processing technique were chosen according to successful results of previous studies (Ishutov et al. 2018a, b), deviations

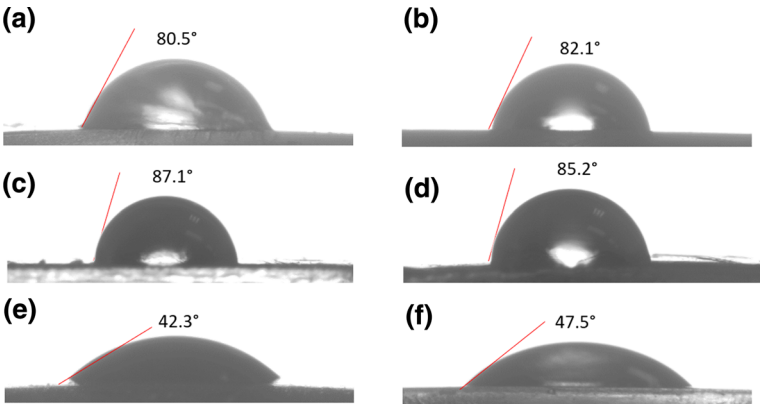

Fig. 5 Results of contact angle measurements between 3D-printed disks and deionized water. Resins: **a** black; **b** gray; **c** clear; **d** white; **e** green; **f** yellow. These angles represent the mean value for each resin calculated from 1000 frames captured by the drop shape analyzer

Table 2 Design characteristics for Fontainebleau sandstone proxy

Magnification	Height (cm)	Length (cm)	Width (cm)	Bulk volume (cm^3)	Porosity (%BV)	Density (g/cm^3)	Mass (g)
15	1.5	1.5	1.5	3.38	12.7	1.09–1.12	3.68–3.79
23	2.3	2.3	2.3	12.17	12.7	1.09–1.12	13.27–13.63
30	3.0	3.0	3.0	27.0	12.7	1.09–1.12	29.43–30.24

Magnification refers to uniform increase in a digital volume from the original 1 mm^3. Bulk dimensions (height, length, width, volume) and porosity are calculated from tomographic data (Ishutov et al. 2018b). Density is provided by vendor's material data sheets. Mass is calculated from tomographic volume and material density. *BV* bulk volume

in 3D-printed bulk volumes could be one of the main contributors to variations in helium porosity (Table 3). Despite the range of magnifications used for this model, all proxies should have shown the same porosity, because the ratio between the pore volume and bulk volume did not change. Nevertheless, flaws in printer's hardware and printing parameters could also result in incomplete manufacture of the pore network reducing the total connected porosity in proxies.

Overall, helium porosity showed a linear trend for all proxies of Fontainebleau sandstone in all magnifications, with a favorable correlation coefficient (R^2) (Fig. 6). R^2 had a range from 0.85 (green proxies) to 0.99 (gray proxies). Proxies 3D-printed in the green resin had the best repeatability and consistency of helium porosity among three magnifications (10.05–11.24%; Table 3).

Bulk volume and mass of proxies 3D-printed in black, gray, and white resins were also close to the designed parameters (Tables 1, 2, 3). Bulk density and resin density were not similar in all samples because the resin density was measured on 3D-printed samples via helium pycnometry (Table 3). Bulk density of all proxies (1.05–1.14 g/cm^3) agreed favorably with vendor data (1.09–1.12 g/cm^3). The highest inconsistency in bulk properties and porosity was found in proxies 3D-printed in the yellow resin (helium porosity of 7.26–11.61%; resin density of 1.23–1.24 g/cm^3). This finding was somewhat counterintuitive, because the yellow

Table 3 Results of helium pycnometry for Fontainebleau sandstone proxies

Resin/magnification	Mass (g)	Height (cm)	Length (cm)	Width (cm)	Bulk volume (cm^3)	Helium porosity (%BV)	Bulk density (g/cm^3)	Resin density (g/cm^3)
Black 15-fold	3.69	1.51	1.49	1.49	3.34	5.5	1.10	1.19
Black 23-fold	13.32	2.29	2.28	2.3	12.01	8.10	1.11	1.19
Black 30-fold	28.21	2.98	2.99	3.01	26.82	12.20	1.05	1.18
Gray 15-fold	3.63	1.51	1.49	1.50	3.36	7.89	1.08	1.19
Gray 23-fold	12.73	2.23	2.29	2.30	11.73	10.42	1.09	1.19
Gray 30-fold	28.51	3.01	2.98	3.00	26.86	12.43	1.06	1.19
Clear 15-fold	3.75	1.48	1.51	1.51	3.38	4.30	1.11	1.19
Clear 23-fold	13.23	2.30	2.31	2.30	12.18	8.44	1.09	1.19
Clear 30-fold	28.71	3.00	3.00	3.00	27.01	11.20	1.06	1.20
White 15-fold	3.81	1.50	1.50	1.50	3.38	5.59	1.13	1.19
White 23-fold	12.92	2.29	2.31	2.30	12.15	10.54	1.06	1.19
White 30-fold	28.51	2.99	3.01	3.00	26.97	11.53	1.06	1.19
Green 15-fold	3.89	1.53	1.49	1.50	3.42	10.05	1.14	1.23
Green 23-fold	13.45	2.32	2.30	2.32	12.32	10.27	1.09	1.20
Green 30-fold	29.21	3.00	3.03	3.00	27.29	11.24	1.07	1.21
Yellow 15-fold	3.94	1.51	1.50	1.52	3.44	7.26	1.14	1.23
Yellow 23-fold	13.54	2.31	2.32	2.28	12.22	10.28	1.11	1.23
Yellow 30-fold	29.70	3.00	3.01	3.02	27.20	11.61	1.09	1.24
SD 15-fold	0.11	0.01	0.01	0.01	0.03	1.89	0.02	0.02
SD 23-fold	0.29	0.03	0.01	0.01	0.19	1.00	0.02	0.02
SD 30-fold	0.50	0.01	0.02	0.01	0.17	0.46	0.01	0.02

SD standard deviation calculated as an average value for all resins at each magnification. Resin density is calculated using grain volumes obtained during helium pycnometry. *BV* bulk volume

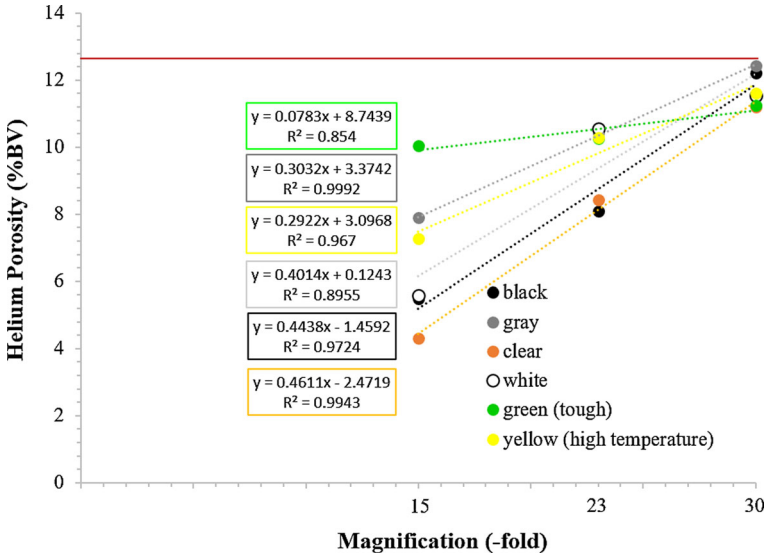

Fig. 6 Results of helium pycnometry from resin proxies of Fontainebleau sandstone. Color in the equation box matches the resin color in the legend. Best fit for dashed trendlines between magnification and helium porosity is linear. Trendline equations and correlation coefficient (R^2) are provided for each resin. Solid red line is a reference to the digital porosity calculated from tomographic volume of Fontainebleau sandstone

resin had the lowest viscosity among all resins tested and hence should have provided a better molecular mobility and better laser penetration.

3.4 Pore-Throat Size Distributions

Mercury intrusion porosimetry is based on using the non-wetting nature of mercury to obtain a pore-throat size distribution for a porous sample. The mercury sample cell could only accommodate the 15-fold proxies for this analysis. Cumulative intrusion curves were generated in this way for six proxies (Fig. 7). Three mode ranges of pore-throat sizes were observed: (1) 0.01–0.05 μm; (2) 10–30 μm; and (3) 320–360 μm. The first range could be explained by the compressibility of the 3D-printed resin at high pressures (> 100 psi; 0.68 MPa) (Ishutov et al. 2017; Hasiuk et al. 2018), which did not represent a geometric feature of the medium. The second range could represent the inner pores that were connected from inside the proxy to its external surface. The third range showed the results of the 3D-printed pore throats that were supposed to conform with the designed pore-throat diameter of 456 μm. The control sample of a solid cube 3D-printed in the black resin showed similar distribution for the first size range.

Proxies 3D-printed in the green resin showed a higher range of incremental pore volume (0.007–0.047 cm^3/g) and more prominent peaks in the pore-throat size distribution than other proxies. In addition, a mode of ~ 80 μm was observed in the distribution plot (Fig. 7). Higher cumulative volume and several mode ranges could be a result of higher connectivity between pores. Given the consistent helium porosity results for green proxies, other magnifications could demonstrate a similar trend in pore-throat size distribution. Proxies 3D-printed in black, clear, and white resins had a similar range of incremental pore volumes, despite different peaks in pore-throat size distribution between 10 μm and 30 μm. Proxies 3D-printed in yellow and

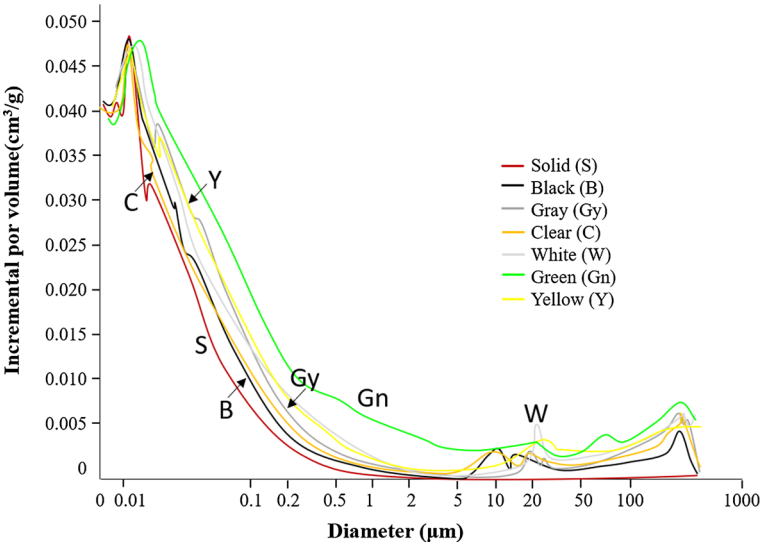

Fig. 7 Pore-throat size distribution measured on Fontainebleau sandstone proxies using mercury porosimetry. Pore-throat diameter modes for each resin: black—325 μm, gray—390 μm, clear—405 μm, white—320 μm, green—330 μm, yellow—320 μm. Solid sample (15-mm cube) was subjected to mercury porosimetry to identify intricate pores inside resins. Each curve is labeled with color and letter

gray resins also showed similar incremental pore volumes. In addition, yellow resin proxies lacked a prominent peak at 320–360 μm. The other five resins showed peaks within this range for pore-throat diameter, but all of the proxies deviated from the designed value (456 μm) by 96–136 μm.

4 Discussion

4.1 Chemical Composition

Prediction of physical, transport, and mechanical properties of proxies in cured SLA resins depends on the knowledge of physical and chemical properties of their uncured counterparts. Two major components of the six resins investigated in this study are monomer and oligomer chains that have active long and short groups at their ends as well as photoinitiators and specialty additives. When the UV laser light in laser passes through the resin, the photoinitiator molecule breaks down into two parts, which become very reactive. These reactive "radicals" connect to the active ends of monomers and oligomers, forming longer polymer chains (Naka 2014). Therefore, the resin solidifies due to growth and cross-linkage of polymer chains. While the bulk composition and polymerization process are similar for all resins, results of this study show that their resulting properties in 3D-printed proxies are different.

Material data sheets of resins provided by the vendor (FormLabs) indicate that green and yellow resins contain acrylated monomers that are absent in the other four resins. Acrylated monomers tend to polymerize faster than methacrylated monomers, which provide lower degrees of lateral strength in a 3D-printed sample (Manzano et al. 2017). Methyalacrylated monomers and oligomers exist in a semi-reacted state, where polymerizable groups of the

resin can form bonds with active components. When the next layer is cured, these semi-reacted polymers attach to the groups of the previous layer, forming bonds both laterally and vertically. These reactions imply that there should be very little difference between vertical and horizontal planes in terms of polymer bonds. Whether isotropy exists at micro- and nanoscales and how it affects mechanical properties and resolution of the resulting proxies remains uncertain and requires advanced imaging techniques (e.g., scanning electron microscopy).

4.2 Viscosity and Temperature

Despite chemical composition, transparency and viscosity were the two properties of uncured resins that could affect accuracy of a proxy. As reported in previous studies (e.g., Ishutov et al. 2018b), the clear resin demonstrated lower accuracy than the black resin due ineffective curing of pore edges by the laser beam during 3D printing. Measurements of bulk properties in this study (Tables 3) corroborated this observation, because clear and black resins had the highest deviations of bulk properties among others. Higher viscosity (970 cps) and higher resin temperature (35 °C) for the green resin provided the most accurate results. Although vendor's specifications suggested that resin temperature should have been close to the room temperature, so that printed proxies would not be affected by thermal expansion and contraction artifacts, this recommendation might not work for all resins. All resins were 3D-printed at the same ambient conditions (room temperature and pressure), but resin temperature affected viscosity and resulting proxy properties. The presence of fast polymerizing acrylated monomers in the green resin in concert with higher printing temperature allowed for higher viscosity. For the yellow resin, which had lower viscosity and the same composition as the green resin, polymerization should have been slower affecting the accuracy of the resulting proxies. Similarity in viscosity among black, clear, white, and gray resins indicated the regular polymerization pattern where oligomers and monomers were linked with each other having active radicals when resins were exposed to the UV light.

4.3 Wettability

The wetting nature of all resins with respect to water was not surprising due to the chemical composition and smoothness of 3D-printed surfaces (Encinas et al. 2010; Baba et al. 2015). Green and yellow resins had lower contact angles, perhaps because of the presence of acrylated monomers polymerizing faster than other resin components. Surface physics of proxies could affect the measurement of contact angles, as seen in the case of the clear resin, which was not smooth (Fig. 5c). Additional treatment of 3D-printed surfaces might be required to eliminate artifacts of 3D printing and post-processing. While this treatment could be time-consuming and it would need further investigation, other studies have shown that wettability could be altered in two ways: (1) by chemically coating cured resin samples to alter the surface (e.g., Gerami et al. 2016; Alzahid et al. 2018) and (2) by modifying the uncured resin composition to match a specific contact angle range (e.g., Manzano et al. 2017). Both scenarios open avenues for future studies on tuning the wettability to a desired state that is similar to natural porous rocks or artificial materials.

Table 4 Results of error calculations for parameters used in Table 3

Resin	Δ Mass (%)	Δ Bulk volume (%)	Δ Porosity (%)	Δ Density (%)	Total Δ	Accuracy
Black	4.18	0.59	32.28	7.24	44.29	Low
Gray	3.66	0.73	19.31	7.53	31.23	Moderate
Clear	2.28	0.04	37.16	7.77	47.25	Low
White	-4.16	0.11	27.37	2.10	33.74	Moderate
Green	2.51	1.11	17.17	0.46	21.25	High
Yellow	2.75	1.01	23.46	11.26	38.48	Moderate

Δ for each property represents a mean value for all magnifications of each resin (mass, bulk volume, porosity and density). Density referred herein is a material (resin) density. Values of Δ are an error for measured and calculated properties of rock proxies in comparison with designed values in Table 2. Total Δ is a sum of all errors for each resin. Accuracy is based on ranking of total Δ

4.4 Ranking Resins for Their Application in Flow and Geomechanical Studies

Considering the bulk properties (mass, bulk volume, density) and pore network replication (porosity) for proxies 3D-printed in six resins from tomographic volume of Fontainebleau sandstone, each resin was ranked for accuracy (Table 4). Values of Δ represented an error for measured and calculated properties of rock proxies in comparison with designed values in Table 2. All errors were added to rank high (<30%), moderate (31–40%), and low (>41%) accuracy based on the total Δ. Resins with the highest ranking represented higher accuracy. The most accurate proxies were printed in the green resin, and the least accurate proxies were printed in the clear resin. This ranking was not conclusive, because mercury porosimetry was not performed on all magnifications and the pore connectivity in larger proxies (23- and 30-fold) was likely better, but remained untested. Nonetheless, all 15-fold proxies had pore-throat modes close to designed 456 μm, which suggested moderate repeatability. While the composition of green and yellow resins was similar, viscosity and resin temperature during 3D printing might result in higher accuracy of rock proxies 3D-printed in the green resin.

Porosity is one of the key properties for characterization of both transport and geomechanical properties of porous media. 15-fold magnification for resin proxies had lower porosities (4–10%) than designed (12.7%) because the smallest pores were not properly printed, and their connectivity was disrupted by inaccurate geometry and stranded pores. 23- and 30-fold magnification for resin proxies showed better conformance of porosity (8–12%) to the designed. High-pressure mercury intrusion for proxies suggested the presence of submicron pores—a result of material compression. These pores did not contribute to the total connected porosity because helium porosity for all resins was lower than designed. They perhaps were formed between layers of the 3D-pritned resin, because the mode for this pore-throat size was close to the layer thickness (50 μm), which represented a gap between layers (Hasiuk et al. 2018). Therefore, the green resin, which had the most uniform results across all magnifications, would take the most magnification to reach 12.7%, while the other resins would reach 12.7% with just a little more magnification than 30-fold.

While all resins tested in this study can find applications in the investigation of transport and geomechanical properties of porous media, their ranking in Table 4 shows the amount of error expected in bulk and pore properties. For example, non-transparent resins (black, green, gray, and white) provide high resolution and accurate replication of fine features (with magnification of the original pore network). In addition, these resins have the highest

tensile strength and flexural moduli (Table 1) which make them suitable for studying both geomechanical and transport properties of natural materials. Transparent resins (clear and yellow) are widely used in imaging flow through etched channels of microfluidic devices; however, geomechanical and coupled flow–geomechanical tests have yet to be performed on these resins. High-temperature and tough resins can be of particular importance for geomechanical testing because of their ability to withstand higher temperatures and pressures, respectively. Considering the lowest deviation in porosity, the highest accuracy (Table 4), and viscosity conformance (Tables 1, 2, 3), the green resin is a good material for replicating natural rock pore networks that can be used in building proxies for experiments with elevated temperatures and pressures and coupled flow–geomechanical studies. Proxies printed in the green resin would be particularly useful in experiments on absolute and relative permeability under various stress conditions. Repeatable tests on replicated pore networks with controlled porosity, wettability, and mechanical properties are a new area in analysis of natural porous media that will help link numerical and experimental modeling.

5 Conclusions

Curable resins used in SLA 3D printing provide avenues for understanding flow and geomechanical processes in porous media. Their physical and chemical properties can be designed to mimic the geomechanical behavior of natural porous rocks during deformation, and their surface physics can be altered to replicate wettability of reservoir rocks. This study presents characterization of uncured resins and proxies 3D-printed from tomographic data of Fontainebleau sandstone to establish the reproducibility of the same pore network in resins with varying physical and chemical properties.

Viscosity of uncured resins is one of the most important properties that determine the resulting polymerization of a 3D-printed model. Rheometer results showed that all resins conformed to the vendor's material data sheets for viscosity (850–900 cps for black, gray, clear, and white resins, 970 cps for the green resin and 600 cps for the yellow resin). Contact angle measurements of water drops on solid disks using the sessile drop method indicated favorable wetting of all resins (all contact angles $< 90°$). If the polymerization was affected by changes in ambient pressure, temperature or humidity and if other non-wetting components were added into those resins, 3D-printed surfaces could become non-wetting with respect to water.

The accuracy of each resin in relation to replication of a natural porous medium was tested by 3D printing proxies of 1 mm^3 tomographic volume of Fontainebleau sandstone at three magnifications (15-, 23-, and 30-fold). Helium pycnometry revealed that 15-fold resin proxies had lower porosities (4–10%) than designed (12.7%). Proxies with 23- and 30-fold magnification showed better conformance of porosity to the designed model (8–12%). Results of mercury porosimetry tests on 15-fold magnification proxies showed that pore-throat sizes were smaller by 96–136 μm than designed (456 μm). High-pressure mercury intrusion for proxies suggested the presence of submicron pores—an artifact of 3D printing, or of material compression, or both. Among all resins tested, the green (tough) resin had the highest accuracy in replication of pore network of Fontainebleau sandstone due to the least deviations in porosity and density from designed parameters. Proxies 3D-printed in white, black, and gray resins could be used for replication of porous media with moderate accuracy and mean pore-throat diameters of 320 μm. Because yellow (high-temperature) and clear resins had the highest deviations in viscosity measured by rheometer from vendor's

specification, further analysis would determine optimal printing parameters (temperature and humidity) for achieving higher accuracy.

Acknowledgements My appreciation is to Dr. Franek Hasiuk from Kansas Geological Survey (Lawrence, Kansas, USA) for thoughtful discussions and help with mercury porosimetry analysis. I thank Mashud Alam from the Department of Apparel, Events, and Hospitality Management (Iowa State University, Ames, USA), for assistance in contact angle measurement of resin samples used in this study. I would also like to thank Dr. Jacqueline Reber for training on the Rheosys Merlin II rheometer (Structure Lab, Iowa State University).

References

Alzahid, Y.A., Mostaghimi, P., Gerami, A., Singh, A., Privat, K., Amirian, T., Armstrong, R.T.: Functionalisation of polydimethylsiloxane (PDMS)-microfluidic devices coated with rock minerals. Sci. Rep. (2018). https://doi.org/10.1038/s41598-018-33495-8

Andrä, H., Combaret, N., Dvorkin, J., Glatt, E., Han, J., Kabel, M., Keehm, Y., Krzikalla, F., Lee, M., Madonna, C., Marsh, M., Mukerji, T., Saenger, E.H., Sain, R.: Digital rock physics benchmarks—part II: computing effective properties. Comput. Geosci. (2013). https://doi.org/10.1016/j.cageo.2012.09.008

ASTM-D7334-08: Standard Practice for Surface Wettability of Coatings, Substrates and Pigments by Advancing Contact Angle Measurement (2013)

Ayub, K.V., Santos, G.C., Rizkalla, A.S., Bohay, R., Pegoraro, L.F., Rubo, J.H., Santos, M.J.M.C.: Effect of Preheating on microhardness and viscosity of 4 resin composites. J. Can. Dent. Assoc. **80**, e12 (2014)

Baba, E.M., Cansoy, C.E., Zayim, E.O.: Optical and wettability properties of polymers with varying surface energies. Appl. Surf. Sci. (2015). https://doi.org/10.1016/j.apsusc.2015.02.150

Bacher, M., Schwen, A., Koestel, J.: Three-dimensional printing of macropore networks of an undisturbed soil sample. Vadose Zone J. (2014). https://doi.org/10.2136/vzj2014.08.0111

Blunt, M.J., Bijeljic, B., Dong, H., Gharbi, O., Iglauer, S., Mostaghimi, P., Paluszny, A., Pentland, C.: Pore-scale imaging and modeling. Adv. Water Resour. (2013). https://doi.org/10.1016/j.advwatres.2012.03.003

Dvorkin, J., Armbruster, M., Baldwin, C., Fang, Q., Derzhi, N., Gomez, C., Nur, B., Nur, A.: The future of rock physics: computational methods vs. lab testing. Pet. Geol. **26**, 63–68 (2008)

Encinas, N., Pantoja, M., Abenojar, J., Martinez, M.A.: Control of wettability of polymers by surface roughness modification. J. Adhes. Sci. Tech. (2010). https://doi.org/10.1163/016942410X511042

Gerami, A., Mostaghimi, P., Armstrong, R.T., Zamani, A., Warkiani, M.E.: A microfluidic framework for studying relative permeability in coal. Int. J. Coal Geol. (2016). https://doi.org/10.1016/j.coal.2016.04.002

Gunda, N.S.K., Bera, B., Karadimitriou, N.K., Mitra, S.K., Hassanizadeh, S.M.: Reservoir-on-a-Chip (ROC): A new paradigm in reservoir engineering. Lab on a Chip (2011). https://doi.org/10.1039/C1LC20556K

Hasiuk, F., Ishutov, S., Pacyga, A.: Validating 3D-printed porous proxies by tomography and porosimetry. Rapid Prototyp. J. (2018). https://doi.org/10.1108/RPJ-06-2017-0121

Ishutov, S., Hasiuk, F.: 3D printing Berea sandstone: testing a new tool for petrophysical analysis of reservoirs. Petrophysics **58**, 592–602 (2018)

Ishutov, S., Hasiuk, F.J., Fullmer, S.M., Buono, A., Gray, J.N., Harding, C.: Resurrection of a reservoir sandstone from tomographic images using 3-D Printing. Am. Assoc. Pet. Geol. Bull. (2017). https://doi.org/10.1306/11111616038

Ishutov, S., Hasiuk, F., Agar, S.M., Jobe, D.: Using resin-based 3D printing to build accurate proxies of porous sedimentary rocks. Groundwater (2018a). https://doi.org/10.1111/gwat.12601

Ishutov, S., Jobe, T.D., Zhang, S., Gonzalez, M.A., Agar, S.M., Hasiuk, F., Watson, F., Geiger, S., Mackay, E., Chalaturnyk, R.: 3D printing for geoscience: fundamental research, education, and applications for the petroleum industry. Am. Assoc. Pet. Geol. Bull. (2018b). https://doi.org/10.1306/0329171621117056

Ju, Y., Zheng, Z., Xie, H., Lu, J., Wang, L., He, K.: Experimental visualisation methods for three-dimensional stress fields of porous solids. Exp. Tech. (2017). https://doi.org/10.1007/s40799-017-0178-1

Lindquist, W.B., Venkatarangan, A., Dunsmuir, J., Wong, T.: Pore and throat size distributions measured from synchrotron X-ray tomographic images of Fontainebleau sandstones. J. Geophys. Res. (2000). https://doi.org/10.1029/2000JB900208

Manzano, J.S., Weinstein, Z.B., Sadow, A.D., Slowing, I.I.: Direct 3D printing of catalytically active structures. Am. Chem. Soc. Catal. (2017). https://doi.org/10.1021/acscatal.7b02111

Matsumura, S., Kobayashi, T., Mizutani, T., Bathurst, R.: Manufacture of bonded granular soil using X-ray CT scanning and 3D printing. Geotech. Test. J. (2017). https://doi.org/10.1520/GTJ20160273

Munro, B., Becker, S., Uth, M.F., Preußer, N., Herwig, H.: Fabrication and characterization of deformable porous matrices with controlled pore characteristics. Transp. Porous Med. (2015). https://doi.org/10.1007/s11242-014-0426-0

Naka, K.: Monomers, oligomers, polymers, and macromolecules (overview). In: Kobayashi, S., Müllen, K. (eds.) Encyclopedia of Polymeric Nanomaterials. Springer, Berlin, Heidelberg (2014)

Ogawa, T., Hasegawa, A.: Effect of curing environment on mechanical properties and polymerizing behaviour of methyl-methacrylate autopolymerizing resin. J. Oral Rehabil. (2005). https://doi.org/10.1111/j.1365-2842.2004.01406.x

Song, W., de Haas, T.W., Fadaei, H., Sinton, D.: Chip-off-the-old-rock: the study of reservoir-relevant geological processes with real-rock micromodels. Lab on a Chip (2014). https://doi.org/10.1039/C4LC00608A

Xu, W., Ok, J.T., Xiao, F., Neeves, K.B., Yin, X.: Effect of pore geometry and interfacial tension on water-oil displacement efficiency in oil-wet microfluidic porous media analogs. Phys. Fluids (2014). https://doi.org/10.1063/1.4894071

Zarikos, I.M., Hassanizadeh, S.M., van Oosterhout, L.M., van Oordt, W.: Manufacturing a Micro-model with integrated fibre optic pressure sensors. Transp. Porous Med. (2018). https://doi.org/10.1007/s11242-018-1000-y

Zhou, T., Zhu, J.B., Ju, Y., Xie, H.P.: Volumetric fracturing behavior of 3D printed artificial rocks containing single and double 3D internal flaws under static uniaxial compression. Eng. Frac. Mech. (2019). https://doi.org/10.1016/j.engfracmech.2018.11.030

Zhou, T., Zhu, J.B.: Identification of a suitable 3D printing material for mimicking brittle and hard rocks and its brittleness enhancements. Rock Mech. Rock Eng. (2017). https://doi.org/10.1007/s00603-017-1335-7

Zhu, J.B., Zhou, T., Liao, Z.Y., Sun, L., Li, X.B., Chen, R.: Replication of internal defects and investigation of mechanical and fracture behaviour of rock using 3D printing and 3D numerical methods in combination with X-ray computerized tomography. Internat. J. Rock Mech. Min. Sci. (2018). https://doi.org/10.1016/j.ijrmms.2018.04.022